A fault-bounded palaeo-lake basin preserved beneath the

Greenland Ice Sheet

3

1

2

Guy J. G. Paxman^{1*}, Jacqueline Austermann¹, Kirsty J. Tinto¹

5 6

¹ Lamont-Doherty Earth Observatory, Columbia University, Palisades, NY 10964, USA

*Corresponding author: Guy J. G. Paxman (gpaxman@ldeo.columbia.edu)

8

7

9 10

This is the accepted manuscript (link to formal publication: 10.1016/j.epsl.2020.116647)

11 12 13

© 2021. This manuscript version is made available under the CC-BY-NC-ND 4.0 license

https://creativecommons.org/licenses/by-nc-nd/4.0/

15

14

16

17 18

19

20

21

22

23

24

25

26

27

28

29

30

31

32

3334

35

3637

Abstract

Subglacial topography not only exerts strong controls on contemporary ice sheet dynamics, but also provides an important long-term record of landscape evolution pertaining to past glacial and interglacial conditions. In particular, the bed topography beneath the Greenland Ice Sheet bears the signatures of past processes of landscape evolution that record the development of the ice sheet since its inception. Here we present evidence from airborne radio-echo sounding, gravity, and magnetic data for an enclosed palaeo-lake basin situated beneath the ice sheet in northwest Greenland. Geomorphological analysis and hydrological modelling indicate that the basin once hosted a lake with a surface area of ~7,100 km² and a volume of ~580 km³. The basin and associated topography control the organisation of a preserved palaeo-fluvial channel network, suggesting that the basin pre-dates widespread glaciation in northwest Greenland. We use flexural modelling to show that the morphology of the basin and surrounding topography is consistent with elastic plate flexure driven by mechanical displacement along a normal fault bounding the basin margin. Analysis of gravity and magnetic anomalies indicates that the basin contains a sedimentary infill up to ~1.2 km thick, which may contain valuable records of past ice sheet extent and environmental conditions in northwest Greenland. We therefore propose that this newly identified palaeolake basin may be a promising target for future acquisition of ground-based active source seismic data and potential recovery of subglacial material by sub-ice drilling programs.

1. Introduction

The Greenland Ice Sheet (GrIS) contains an ice volume equivalent to ~7.4 m of global sea level rise (Morlighem et al., 2017). Loss of ice from Greenland due to ongoing and projected future climate and ocean warming therefore has the potential to cause substantial global societal impacts. In northwest Greenland, satellite radar altimetry measurements have revealed notably high (up to ~1 m/yr) rates of ice surface thinning during the past two decades (The Imbie Team, 2020). Moreover, numerical ice sheet modelling studies predict that the glacier catchments in northwest Greenland are likely to be among the first to undergo accelerated mass loss in response to projected future oceanic and atmospheric warming (Fürst et al., 2015; Pattyn et al., 2018). While northwest Greenland will potentially be a significant contributor to global sea level rise in the coming decades, the likely rate and magnitude of this change remain uncertain.

To this end, better constraining the behaviour and extent of the GrIS in northwest Greenland during past warm periods can aid our understanding of its response to current and projected future warming. However, the long-term glacial history of northwest Greenland remains relatively unresolved. While offshore sediment and oxygen isotope records suggest that ice in the Northern Hemisphere experienced a major expansion during the Pliocene (Miller et al., 2020), there is also fragmentary evidence for regional land-based ice in Greenland since the Miocene (Helland and Holmes, 1997) or even as early as the late Eocene (Eldrett et al., 2007; Tripati and Darby, 2018).

In northwest Greenland, ice sheet model ensembles indicate a wide range of possible ice sheet extents during the mid-Pliocene warm period (ca. 3.26-3.02 Ma), the most recent interval when atmospheric CO₂ levels were comparable to today (~400 ppm) (Koenig et al., 2015). Seismic surveying of the northwest Greenland continental shelf has revealed progradational sedimentary units that record 11 cycles of ice advance and retreat since the Pliocene, indicative of a dynamic and fluctuating ice margin (Knutz et al., 2019). Largely icefree conditions during parts of the Pliocene and early Pleistocene have been invoked based on marine sediments of the Kap København Formation in northern Greenland, which contain fossilised wood and macrofauna that support the presence of boreal forests and summer temperatures 6-8 °C higher than today (Bennike et al., 2010; Funder et al., 2001). Cosmogenic nuclide surface exposure dating from a bedrock core beneath the GrIS summit suggests that much of Greenland, including the northwest, was ice-free for multiple interglacial periods during the Pleistocene (Schaefer et al., 2016), although cosmogenic isotopes in offshore sediments suggest that an ice sheet has persisted in east Greenland for the past 7.5 Myr (Bierman et al., 2016), underlining the ongoing uncertainty surrounding GrIS history.

As a region of potentially significant past, present, and future glacial change, the subglacial topography of northwest Greenland may offer a crucial, yet largely untapped, record for understanding landscape development, past tectonic and surface processes, and past ice sheet behaviour and extent (e.g. Jamieson et al., 2014). For example, palaeo-fluvial landscapes have been documented beneath the Jakobshavn Isbræ and Humboldt Glacier catchments and it has been suggested that the fluvial network influenced the development of contemporary glacial dynamics (Cooper et al., 2016; Livingstone et al., 2017). More than 600,000 line-km of radio-echo sounding (RES) data have been acquired over Greenland, the majority of which were collected by the NASA Operation IceBridge (OIB) mission (Paden et al., 2019). Despite this relative wealth of bed elevation measurements, efforts to understand the evolution of Greenland's subglacial landscape have been comparatively limited.

In this study, we aim to constrain the processes involved in the origin and evolution of the subglacial topography of northwest Greenland. We use Operation IceBridge airborne RES, gravity and magnetic datasets, together with geomorphological, flexural, and potential field analysis, to characterise the subglacial landscape and its underlying geological structure. We use our results to assess the implications for past ice sheet behaviour and extent, environmental conditions, and palaeoclimate prior to and during the history of glaciation in northwest Greenland.

2. Observations

In northwest Greenland, the GrIS can be divided into two major glacial drainage catchments separated by an ice divide trending approximately SE–NW (Zwally et al., 2012) (Fig. 1). The catchment to the NE of the ice divide is drained by the Hiawatha, Humboldt and Petermann glaciers, which terminate in the Nares Strait. To the SW of the ice divide, the GrIS is drained by a series of parallel outlets including the Gade, Döcker Smith, Rink, King Oscar, Nansen, and Sverdrup glaciers, which flow into Melville Bay (Fig. 1a). Ice surface velocities close to the ice divide are typically <20 m/yr, and gradually accelerate as ice flow converges and is focussed into fast-moving glaciers, whose velocities commonly exceed 1000 m/yr at the grounding line (Fig. 1a) (Joughin et al., 2010). Bedrock exposure in the region is confined to isolated outcrops between the major outlet glaciers around the coast (Fig. 1). In these areas, the bedrock geology is dominated by crystalline Archaean and Proterozoic gneisses, with localised outcrops of Early Palaeozoic carbonates and siliciclastic sedimentary rocks exposed to the west of Humboldt Glacier (Henriksen et al., 2009).

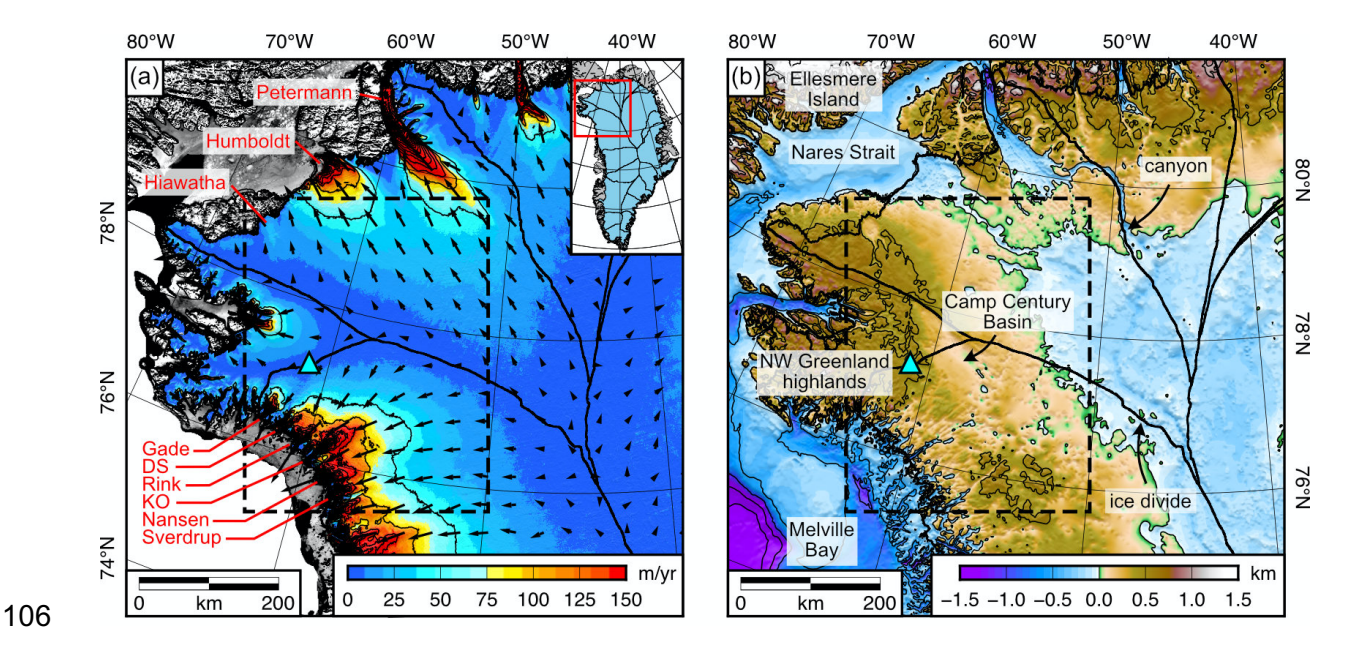


Figure 1. Regional setting. (a) Ice surface velocity (Joughin et al., 2010). Arrows show the direction of the velocity vector, with arrow length scaled to the magnitude of the velocity. Contour interval is 50 m/yr to demarcate regions of fast-flowing ice. Black lines mark the ice drainage divides (Zwally et al., 2012). Major outlet glaciers are labelled (DS = Döcker Smith Glacier; KO = King Oscar Glacier). Blue triangle marks the Camp Century drill-core site. Dashed box marks the extent of Fig. 2. Inset marks the study area within Greenland. (b) Bed topography / bathymetry (Morlighem et al., 2017) with major geographical features labelled. Elevations are relative to mean sea level under modern ice conditions (i.e. loaded by the GrIS). Contour interval is 500 m.

Bed elevation measurements show that the major outlet glaciers in northwest Greenland are underlain by deep subglacial troughs up to ~30 km wide and ~1000 m below sea level (Morlighem et al., 2017). These troughs have likely been selectively excavated as ice flow is focussed through these outlets and drains towards the ice sheet margin (Kessler et al., 2008; Medvedev et al., 2013). Upstream of the Humboldt and Petermann glaciers, the subglacial landscape exhibits a network of palaeo-fluvial channels and canyon systems (Fig. 1b) (Bamber et al., 2013; Livingstone et al., 2017; van der Veen et al., 2007). To the southwest, the subglacial topography rises up to a ~200 km-wide highland region that trends parallel to the coast (Fig. 1b) and reaches elevations of up to 1200 m above sea level. These highlands are dissected on their coastal side by a series of linear glacial troughs oriented transverse to the coast (Fig. 1b) (Morlighem et al., 2017). Inland of these troughs is the site of the former Camp Century base (Fig. 2), where an early ice drill-core record was recovered (Weertman, 1968).

Situated immediately to the north of the Camp Century ice core site and beneath the regional ice divide is a conspicuous linear topographic depression, oriented NW–SE (parallel to the ice divide), 20–60 km wide and ~160 km in length (Fig. 2). The basin edges show a marked asymmetry, with a gently sloping SW margin contrasting a steep ~400 m-high escarpment on the NE margin (Fig. 2). The basin flank on the NE margin is characterised by

a tilted surface that dips gently away from the basin towards the palaeo-fluvial subglacial drainage system upstream of Humboldt Glacier (Livingstone et al., 2017). The basin (hereafter referred to as the 'Camp Century Basin') is also situated close to two circular-shaped bedrock depressions that have recently been interpreted as meteorite impact craters (Fig. 2a) (Kjær et al., 2018; MacGregor et al., 2019). The Camp Century Basin forms the focal point of the geomorphological analysis and geophysical modelling in this study.

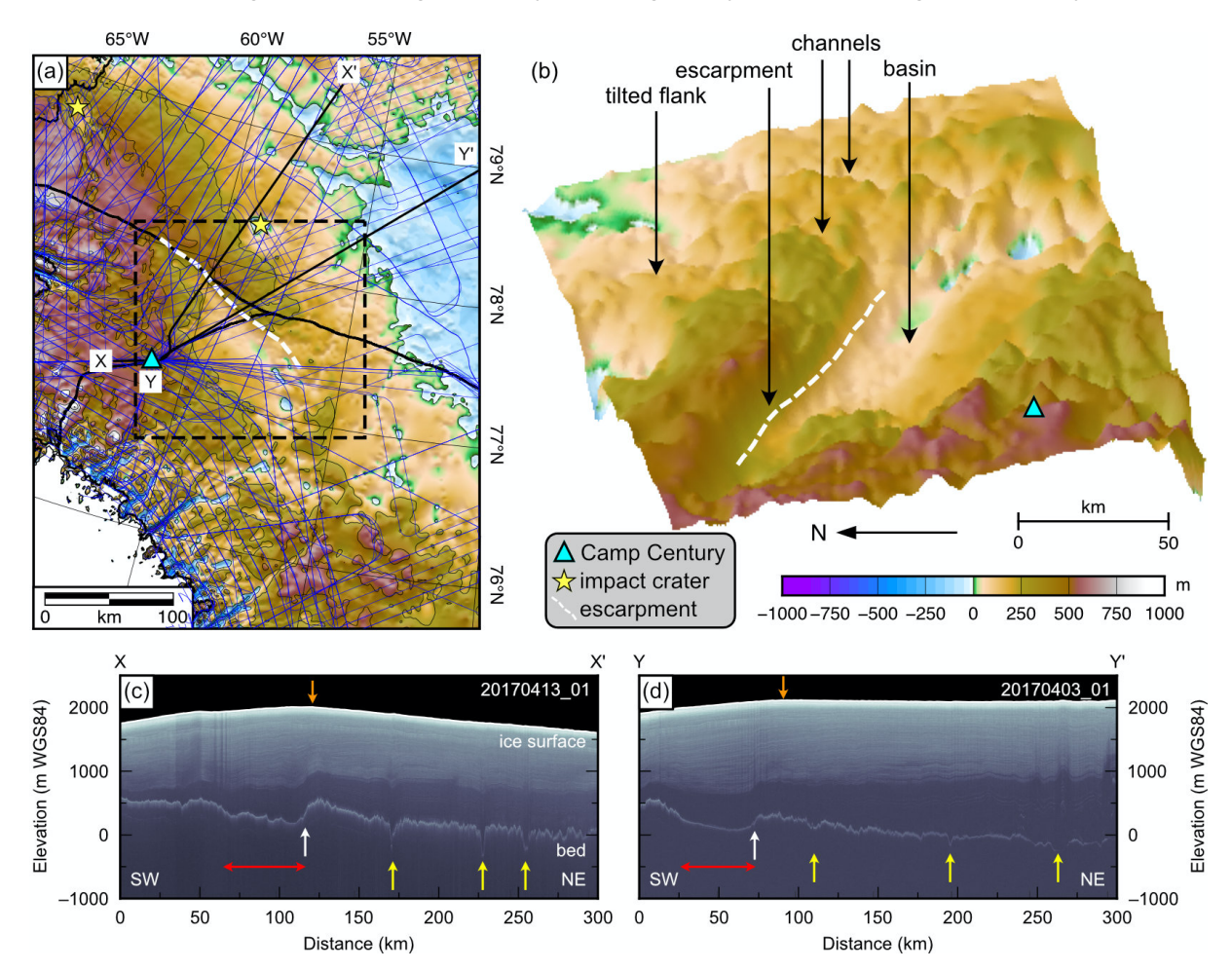


Figure 2. Subglacial topography of northwest Greenland. (a) Digital elevation model (DEM) of regional subglacial topography (Morlighem et al., 2017). Bed elevations are relative to mean sea level under modern ice conditions (i.e. loaded by the GrIS). Blue triangle marks Camp Century. Thick black lines mark the ice drainage divide (Zwally et al., 2012). Thin blue lines show Operation IceBridge (2010–17) flight lines. (b) Perspective image of the DEM from panel a looking along the Camp Century Basin from an azimuth of 285°, with major topographic features labelled. Image extent is marked by the dashed box in panel a. (c) and (d) Operation IceBridge radar echograms along profiles X–X' and Y–Y' (profile locations shown in panel a). Echo elevations are given relative to the WGS84 ellipsoid. The strongest reflectors are the ice surface and bed reflections. The red arrows show the extent of the Camp Century Basin, white arrows mark the escarpment, and yellow arrows mark channels in the associated tilted flank; orange arrows mark the ice divide.

3. Methods

3.1. Subglacial topographic and geomorphological mapping

Subglacial geomorphology offers a powerful insight into the tectonic and surface processes involved in the development of a subglacial landscape. In this study, the BedMachine version 3 digital elevation model (DEM) (hereafter 'BedMachine3') (Morlighem et al., 2017) was used to describe and map geomorphological features visible in the subglacial landscape of northwest Greenland. We also produced a rebounded bed DEM by accounting for the flexural rebound of the subglacial topography following the removal of the entire modern ice sheet load. We computed the flexure using an elastic plate model (see Appendix A), incorporating a spatially variable effective elastic thickness (T_e) model previously derived for Greenland (Supplementary Fig. 1) (Steffen et al., 2018).

Alongside the rebounded bed DEM, along-track bed elevation data from available OIB flight lines (2010–17) (Paden et al., 2019) were used to facilitate our analysis of subglacial geomorphology. Over typical inland subglacial terrain, the OIB RES data are able to resolve bed features down to a width of ~25 m with an elevation uncertainty of ~10–20 m (Paden et al., 2019). In addition, a measure of along-track bed roughness (*v*) was determined by computing the root mean squared (RMS) deviation (Cooper et al., 2019; Shepard et al., 2001) of the bed elevation along OIB flight tracks over a discrete length scale of 800 m, which is appropriate for macro-scale analysis of subglacial topography.

172
$$v(\Delta x) = \left[\frac{1}{N} \sum_{i=1}^{N} [z(x_i) - z(x_i + \Delta x)]^2\right]^{\frac{1}{2}}$$
 (1)

where z is the bed elevation, x is the along-track distance, and Δx is the step size between bed elevation measurements.

We obtained additional independent constraints on subglacial topography using variations in surface brightness as detected in the Moderate-Resolution Imaging Spectroradiometer (MODIS) Mosaic of Greenland (Supplementary Fig. 2) (Haran et al., 2018). These variations in brightness largely reflect small-scale variations in ice surface elevation/morphology, which in turn often originate from subglacial topographic relief that is translated into relatively subtle ice surface expressions, particularly in regions of minimal ice flow and deformation (Ross et al., 2014). MODIS imagery can therefore provide additional information on the spatial distribution and continuity of subglacial features that may otherwise not be easily detectible using RES profile data alone.

3.2. Hydrological flow routing

The pattern of preserved subglacial valley networks can be used to understand the regional topographic controls on pre-glacial hydrological routing, and ascertain the degree to which inherited drainage systems have been modified by subsequent glacial processes (Jamieson et al., 2014). We extracted the ice-free drainage network from the rebounded BedMachine3 DEM by assuming that surface water is routed down the path of steepest

descent within the landscape. Prior to the hydrological routing calculation, internal 'sinks' within the DEM were filled to remove enclosed topographic lows (basins) that would otherwise cause discontinuities in the calculated flow network. These hydrological sinks provide an important measure of the spatial distribution and depth of potential depocentres within the landscape. In our study area the BedMachine3 DEM was produced by interpolation of ice thickness line data derived from a dense network of RES flights (Morlighem et al., 2017) (Fig. 2a, Supplementary Fig. 2), meaning the derived hydrological network is likely to be robust.

3.3. Flexural modelling

The northeast flank of the Camp Century Basin is tilted away from the basin (Fig. 2c,d), with a curved profile exterior to the basin similar to flanks formed by flexural uplift in many continental settings (e.g. Weissel and Karner, 1989). To test the hypothesis that the basin flank has been tilted by flexural uplift, we adopted a 2D modelling approach to compare the observed topography to the predictions of a simple elastic plate model.

We first constructed a representative 'ensemble-averaged' profile of the bed topography crossing the Camp Century Basin and associated escarpment and tilted flank. We sampled 20 evenly spaced parallel profiles from the rebounded BedMachine3 DEM oriented orthogonally to the trend of the basin. These profiles were used to compute the ensemble-averaged topography profile. Ensemble averaging is a spectral technique in which the frequency spectra of an ensemble of profiles are computed using a fast Fourier transform, averaged in the frequency domain, and converted back to an average profile in the spatial domain (Bassett and Watts, 2015). The ensemble average enhances features common to all profiles (e.g. steep escarpments and tilted surfaces), while suppressing the more localised features unique to individual profiles (e.g. valley incision and smaller-scale surface roughness).

We then compared the ensemble-averaged topographic profile to the predictions of a 2D elastic plate model for flexural uplift. In glaciated settings, the two mechanisms commonly invoked for trough formation and adjacent flexural uplift are (i) mechanical unloading due to displacement along a normal fault, and (ii) erosional unloading due to removal of rock by glacial incision. Here we primarily focussed on scenario (i), and used a model in which displacement on a normal fault causes mechanical unloading and flexural uplift of the footwall block via removal of the hanging-wall (see Appendix A). Flexure was computed using a finite difference method (Contreras-Reyes and Osses, 2010), with the effective elastic thickness of the lithosphere (T_e) set to a constant value for the footwall block and decreased to zero at the fault to simulate a plate break. We calculated the load geometry assuming a typical normal fault dip of 60° and a faulted layer thickness of 20 km, which was chosen to match the amplitude of the observed flank uplift. For scenario (ii), shown in the

supplementary material, we used the subglacial topography to estimate the average depth of the Camp Century Basin relative to its surroundings, and assumed that this 'missing' material was removed by erosion, resulting in flexural uplift of the basin flanks. For both scenarios we assumed crust and mantle densities of 2700 and 3330 kg m⁻³ respectively, and varied T_e in an attempt to match the observed topography.

3.4. Gravity modelling and magnetic depth-to-source analysis

227

228

229

230231

232

233234

235

236

237

238

239

240

241242

243

244

245

246

247

248

249250

251

252

253

254

255256

257

258

259

260

261

262

263

While subglacial bedrock geology cannot be mapped in the field or by satellite imagery, potential field data provide valuable insights into the subglacial geological and tectonic structure. To estimate sedimentary thickness, we performed 2D gravity modelling along seven favourably oriented OIB lines crossing the Camp Century Basin, supported by magnetic depth-to-source analysis (airborne free-air gravity and magnetic anomaly data were acquired during the 2011–2012 OIB field seasons (Cochran et al., 2012; Tinto et al., 2019)).

For each model profile, our procedure was to first compute the gravity effects of the ice surface and bed topography (i.e. the Bouguer correction), assuming densities for air, ice, and bedrock/crust of 0, 920, and 2700 kg m⁻³ respectively. A bedrock density of 2700 kg m⁻³ was chosen to reflect the approximate density of the Proterozoic crystalline gneisses that outcrop along the ice margin in this region (Henriksen et al., 2009) and are assumed to occur widely beneath the ice sheet. We then attempted to match long-wavelength (>100 km) trends in the Bouquer anomaly (free-air anomaly minus the Bouquer correction) by forward modelling the geometry of the Moho. We first constrained the Moho model for a reference profile outside the proposed basin, for which we assumed a uniform bedrock density and therefore a Bouquer anomaly arising entirely from the undulation of the Moho. We assumed a mantle density of 3330 kg m⁻³ and an average Moho depth of 38 km below sea level to match the average depth recovered from seismic wave receiver functions and tomography models in northern Greenland (Dahl-Jensen et al., 2003; Pourpoint et al., 2018). We then applied this Moho model to the six profiles that crossed the Camp Century Basin and attempted to reconcile any residual short-wavelength (<100 km) gravity anomalies by forward modelling the geometry of a low-density sedimentary layer within the basin. We used a bulk sediment density of 2400±100 kg m⁻³, assuming that any sedimentary material beneath the ice sheet would be relatively well compacted.

Magnetic anomalies depend on the depth and susceptibility of the magnetic source rocks, providing an independent constraint on subglacial geology. We derived 'depths to magnetic source' along the selected OIB lines using Werner deconvolution, assuming that sedimentary infill has negligible magnetic susceptibility and the surrounding bedrock (e.g. crystalline gneiss) constitutes the magnetic basement. The depth to magnetic source can therefore be interpreted as the depth to the base of a sedimentary sequence. Werner deconvolution considers a range of wavelengths by passing a moving window along the

magnetic anomaly profile. We incrementally increased the window size from 2 to 100 km, which correspond to the highest and lowest frequencies observed magnetic anomalies respectively. This allowed us to recover the estimated depths and magnetic susceptibilities of the source bodies giving rise to magnetic anomalies within this waveband. We then removed any solutions located within or below the ice sheet with negligible susceptibilities (<10⁻¹⁰), which were deemed unlikely to be robust.

4. Results

4.1 Subglacial topography and geomorphology

The OIB radar data and BedMachine3 DEM confirm the presence of an elongate subglacial basin near Camp Century (Fig. 3). The width of the Camp Century Basin increases from 20 km at the northwest end to 60 km near its southeastern limit. The basin floor is situated beneath ~1.8 km of ice at an elevation of ~100 m above present-day sea level (~500 m under ice-free conditions; Fig. 3a). Basal roughness measurements from RES data show that much of the floor of the Camp Century Basin is notably smooth and lacking in incision compared to the surrounding terrain, with low along-track RMS deviations of <10 m within the basin compared to higher values of >20 m across the rest of the region (Fig. 3c). The ice above the basin is characterised by a markedly smooth and featureless surface as imaged by MODIS (Fig. 3b), the outline of which correlates well with the limits of the smooth subglacial topography of the basin floor.

On its northeast margin, the Camp Century Basin rises up a steep ~400 m escarpment to an inclined plateau-like surface that gently dips inland for ~200 km (Fig. 2, 3). The tilted plateau is incised by a number of V-shaped channels (Fig. 3d,e). Mapping of these channels using RES line data, the rebounded BedMachine3 DEM, and MODIS surface imagery revealed a dendritic network of valleys, with several tributary channels nucleating close to the Camp Century Basin escarpment, running NE down the tilted flank away from the basin, and gradually coalescing to form a single major channel (Fig. 3a,b). As well as these 'dip slope channels', we mapped a number of channels that instead cut through the escarpment and drop down into the Camp Century Basin (Fig. 3a,b). These 'scarp channels' are short (<20 km) and either cut directly through the escarpment or can be traced along ramps in the escarpment. The drainage divide between the 'dip slope' and 'scarp' channels follows the crest of the basin flank (Fig. 3a,b).

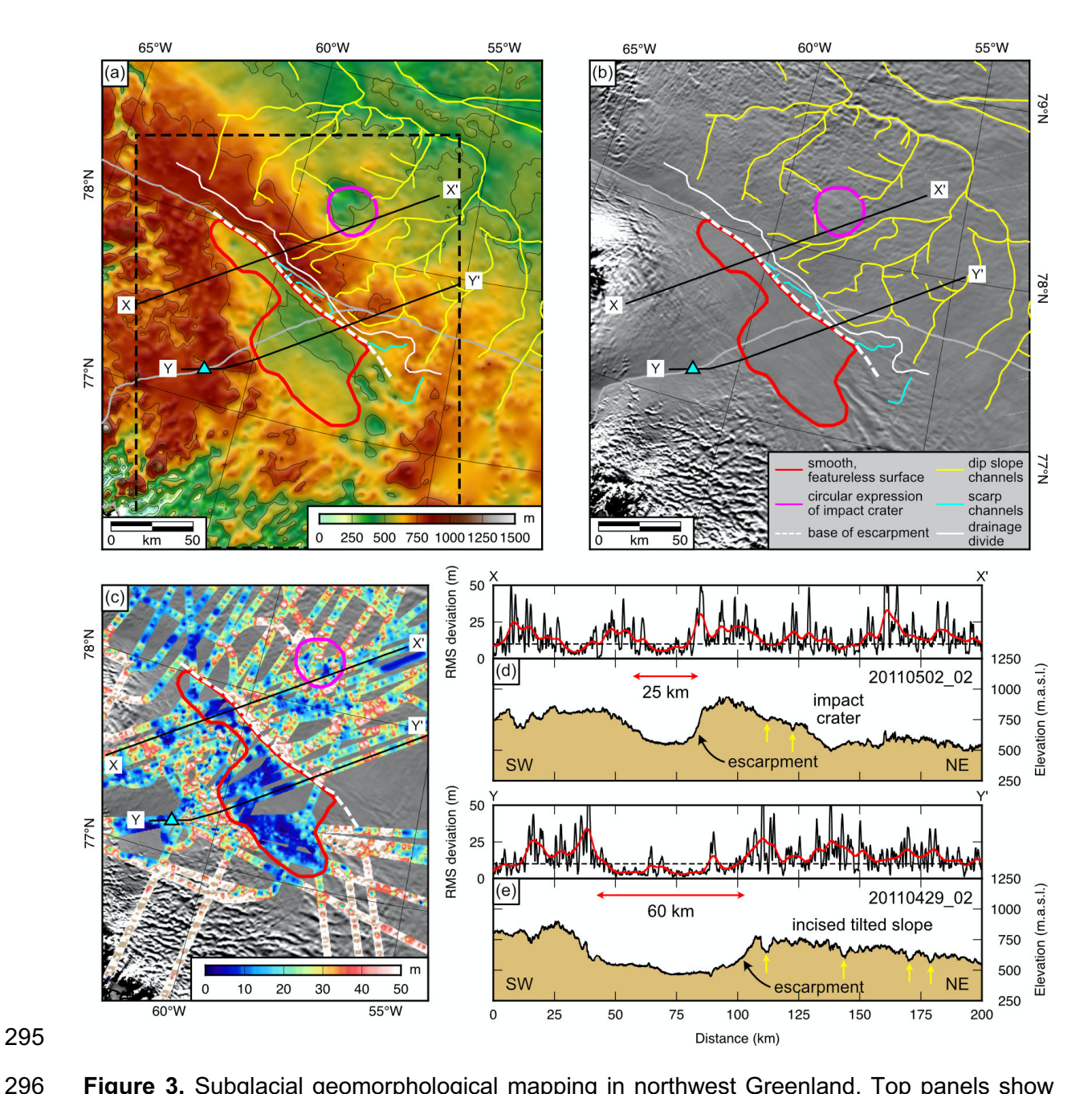


Figure 3. Subglacial geomorphological mapping in northwest Greenland. Top panels show major geomorphological features overlain on (a) rebounded bed topography, and (b) MODIS ice surface imagery. Blue triangle marks Camp Century. Grey lines mark the ice drainage divide (Zwally et al., 2012). The subglacial valley network on the NE flank of the Camp Century Basin can be divided into 'dip slope channels' (yellow) that can be mapped moving NE down the tilted flank and 'scarp channels' (blue) that cut through the escarpment (white dashed line) and into the basin. Dashed box in panel a marks the extent of panel c. (c) RMS deviation of bed elevation along OIB flight tracks, which is a proxy for the roughness of the subglacial terrain. The red outline marks the region of low basal roughness within the Camp Century Basin that corresponds to smooth, featureless surface ice. (d) and (e) OIB profiles crossing the Camp Century Basin X-X' and Y-Y'. Lower panels show rebounded bed elevation (relative to mean sea level). Yellow arrows mark the mapped channels crossed by each profile. The upper panels show along-track RMS deviations; black line = raw values, red line = smoothed values produced using a 10 km Gaussian filter. The basin centre exhibits RMS deviations below 10 m (dashed line), which are indicative of notably smooth terrain.

297

298

299

300

301

302

303

304

305

306 307

308

309

310

The hydrologically derived ice-free drainage network (Fig. 4) yields a distribution of streams that closely resembles the mapped channels both on the dip slope and dissecting the escarpment, and also exhibits a drainage divide along the crest of the flank on the NE side of the basin. This agreement indicates that the hydrological flow routing algorithm provides a realistic prediction of the pathways taken by surface water under ice-free conditions. The drainage algorithm also shows that the Camp Century Basin is a hydrological sink, and would have to fill to a constant level in order to allow water to drain out of the basin (Fig. 4a). The result is a modelled lake with a surface elevation of ~640 m above sea level and an average depth of 82 m. In the northern, narrower part of the lake, the maximum water depth is relatively constant at ~100 m across the basin. To the south, the basin shows a more pronounced asymmetry, with water depths of up to ~250 m near the NE margin, compared with much shallower depths of ~50 m on the SW side of the basin (Fig. 4a). In the hydrological model, the lake is fed by 18 inlet stream channels and has at least one outlet at its southern end that can be traced down to the coast through the subglacial trough that underlies King Oscar Glacier (Fig. 4a).

Notably, several topographic profiles reveal that the gently sloping SW margin of the Camp Century Basin is characterised by flat, terrace-like surfaces and/or breaks of slope situated at consistent elevations of ~650 m above sea level (when ice-free). The 'terraces' comprise a flat or low-angle bed surface measuring up to ~4 km across, which is backed by a steep ~60–80 m-high cliff (Fig. 4; Supplementary Fig. 3). Profiles towards the northern end of the basin show that the elevation of the terraces corresponds very closely to the elevation of the hydrological lake surface (Fig. 4b,c). Towards the southern end of the basin, the bathymetric profile is characterised by a broad, flat platform, which is backed by an abrupt break of slope that coincides with the modelled lake surface (Fig. 4e).

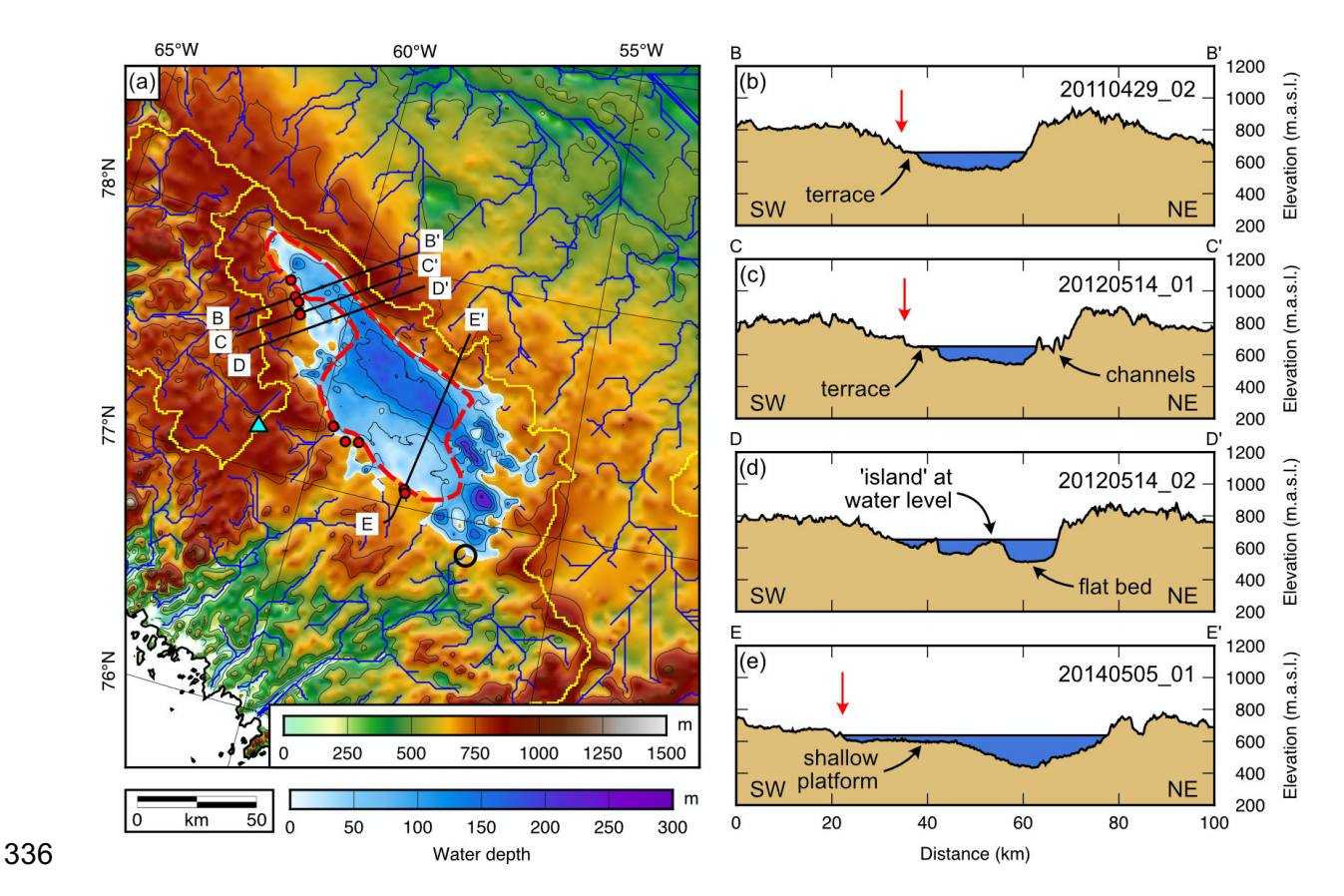


Figure 4. Modelled ice-free hydrological drainage network. (a) Hydrological flow routing network overlain on the rebounded subglacial topography. Blue triangle marks Camp Century. Blue lines mark drainage channels; yellow lines mark drainage divides. The blue coloured region marks the depth of the modelled hydrological lake that fills the Camp Century Basin. The lake outlet is circled in black. Red circles mark the location of terraces and cliffs near the lake shoreline as identified in RES data. Dashed red outline marks the region of low basal and ice surface roughness shown in Fig. 3. (b–e) Rebounded bed elevation along sections of OIB flight lines crossing the Camp Century Basin. Original radar echograms for these lines are displayed in Supplementary Fig. 3. The area in blue represents the modelled lake. Red arrows mark the position of cliffs that back the flat terraces and platforms on the SW margin of the Camp Century Basin.

4.2 Flexural and potential field modelling

The stack of parallel topographic profiles crossing the study area (Fig. 5) shows a well-developed escarpment on the NE margin of the Camp Century Basin. Moreover, the ensemble-averaged bed profile reveals an asymmetrically shaped basin and the typical flexural form of a footwall uplift associated with normal faulting, with a steep \sim 400 m-high escarpment and gently tilted flank (Fig. 5). Comparison of the ensemble-averaged topographic profile with the predictions of an elastic plate model indicate that the form of the bed topography is consistent with flexure due to unloading along a normal fault that coincides with the steep escarpment on the NE flank of the basin (Fig. 6a,b). The value of T_e that produces the closest match with the observed amplitude and wavelength of the tilted flank and thereby minimises the RMS misfit between the topography and the flexural profile is 35 km (Fig. 6a). Lower T_e values cannot explain the broad wavelength (\sim 200 km) of the tilted

NE flank, and erosional unloading alone cannot explain the high amplitudes, steep tilt, and pronounced asymmetry of the uplift (Fig. 6a; Supplementary Fig. 4). Although the modelled fault dip and faulted layer thickness are not independently constrained, sensitivity testing (Supplementary Fig. 5) shows that a trade off between these parameters affects the amplitude of flexure but not the wavelength, which is instead sensitive to (and used to constrain) $T_{\rm e}$ (Fig. 6). We also note that the flexure calculation would be modified by the incorporation of footwall escarpment erosion and concomitant sediment deposition within the basin (Olive et al., 2014), but these processes are difficult to constrain in this setting and are not expected to significantly modify the first order pattern of flexure.

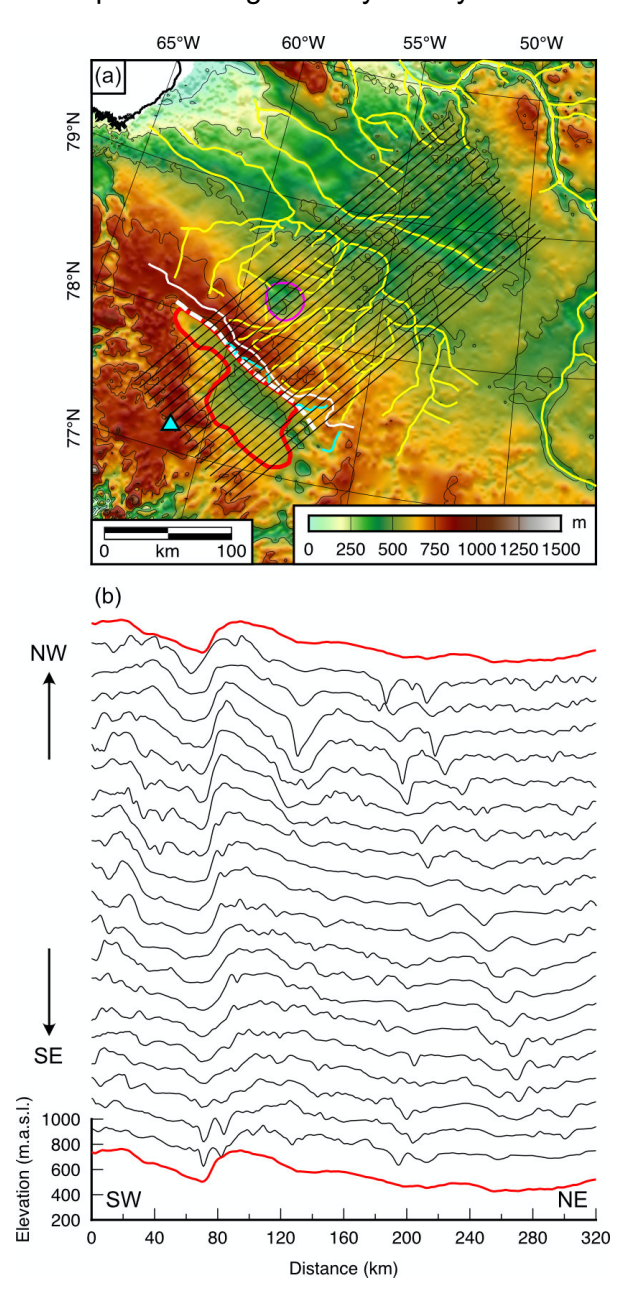


Figure 5. Calculation of the ensemble-averaged topography profile in northwest Greenland. (a) Rebounded bed topography DEM with the locations of the profiles that were ensemble-averaged. The symbology is identical to Fig. 3a. (b) Topography profiles crossing the Camp Century Basin, escarpment, and tilted flank. The black lines show the rebounded bed topography along the profiles shown in panel a and the red lines show the ensemble-

averaged profile (both lines are identical). Profiles are oriented SW–NE (bottom left to top right in panel a) and are stacked with NW to the top and SE to the bottom. The ensemble average reveals an asymmetrically shaped basin, an escarpment on the NE margin, and the typical flexural form of a footwall uplift associated with normal faulting.

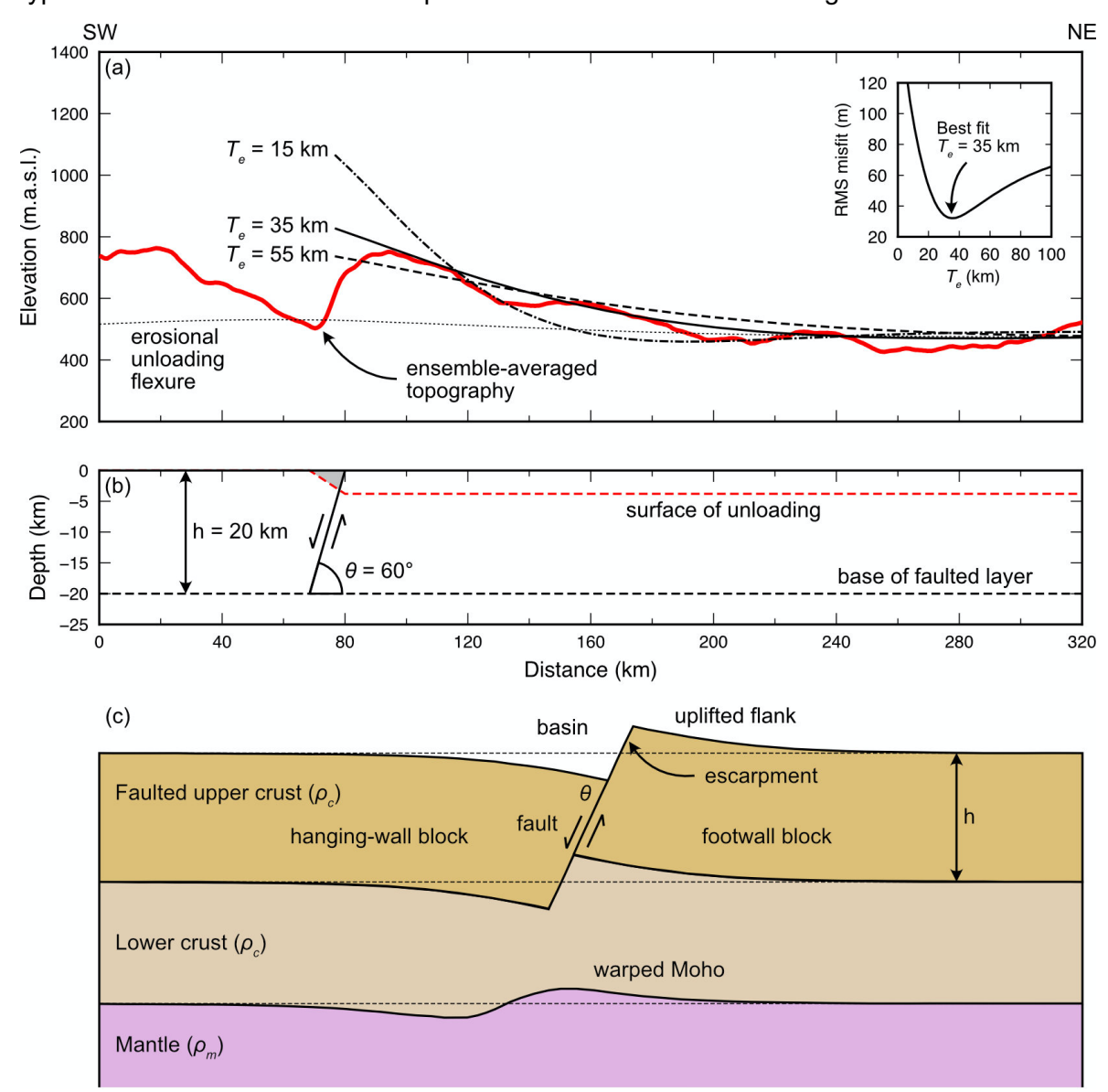


Figure 6. Flexural modelling. (a) Comparison of the ensemble-averaged bed topography profile to a flexural model of mechanical unloading on a normal fault bordering the escarpment on the NE margin of the Camp Century Basin. Red line = ensemble-averaged topography; solid and dashed black lines = calculated footwall uplift for the model geometry shown in panel b for three different values of T_e (15, 35, and 55 km). Inset shows the RMS misfit between the ensemble average and modelled topography profiles for T_e values between 0 and 100 km, revealing a best-fitting value of 35 km. Also displayed is the flexural uplift expected if the basin were formed by erosion (assuming a T_e of 35 km; Supplementary Fig. 4). (b) Fault model and unloading geometry. We assumed a single, purely normal fault positioned below the escarpment in panel a with a typical dip (θ) of 60° and faulted layer thickness (h) of 20 km. The grey wedge-shaped region represents the effective unloading experienced by the footwall block due to downward displacement of the hanging-wall block via slip on the fault. The region is bounded by Earth's surface, the fault, and the surface of unloading (the elevation of the Moho under isostatic equilibrium in the absence of the crust)

(Watts, 2001). (c) Schematic diagram showing the displacement of the surface, crust, and Moho associated with mechanical unloading on a normal fault.

In our forward gravity modelling approach, we were able to account for the long-wavelength trend in the Bouguer anomaly with a crustal model in which (i) the Moho is gently inclined below the NE flank of the Camp Century Basin, mirroring the bed topography, and (ii) the crust thickens by ~4 km on the SW side of the basin (Fig. 7). The warping of the Moho that matches the observed Bouguer anomaly in the reference gravity model outside the basin (profile 1 in Fig. 8) is consistent with the predictions of the normal fault flexure model, where the upward flexed topography of the footwall is associated with a flexed Moho (Fig. 6c), giving rise to the conspicuous (~100 km-wide) gravity anomaly 'high' observed over the flank (Fig. 7b, 8). Moreover, the broad decrease in the gravity anomaly moving NE to SW across the basin (Fig. 7b, 8) is consistent with a deepening of the Moho across the extension of the fault at depth, as predicted by the normal fault model (Fig. 6c). The modelled Moho depth variation is also in close agreement with the seismic Moho derived independently from ambient noise and earthquake surface wave tomography (Fig. 7c).

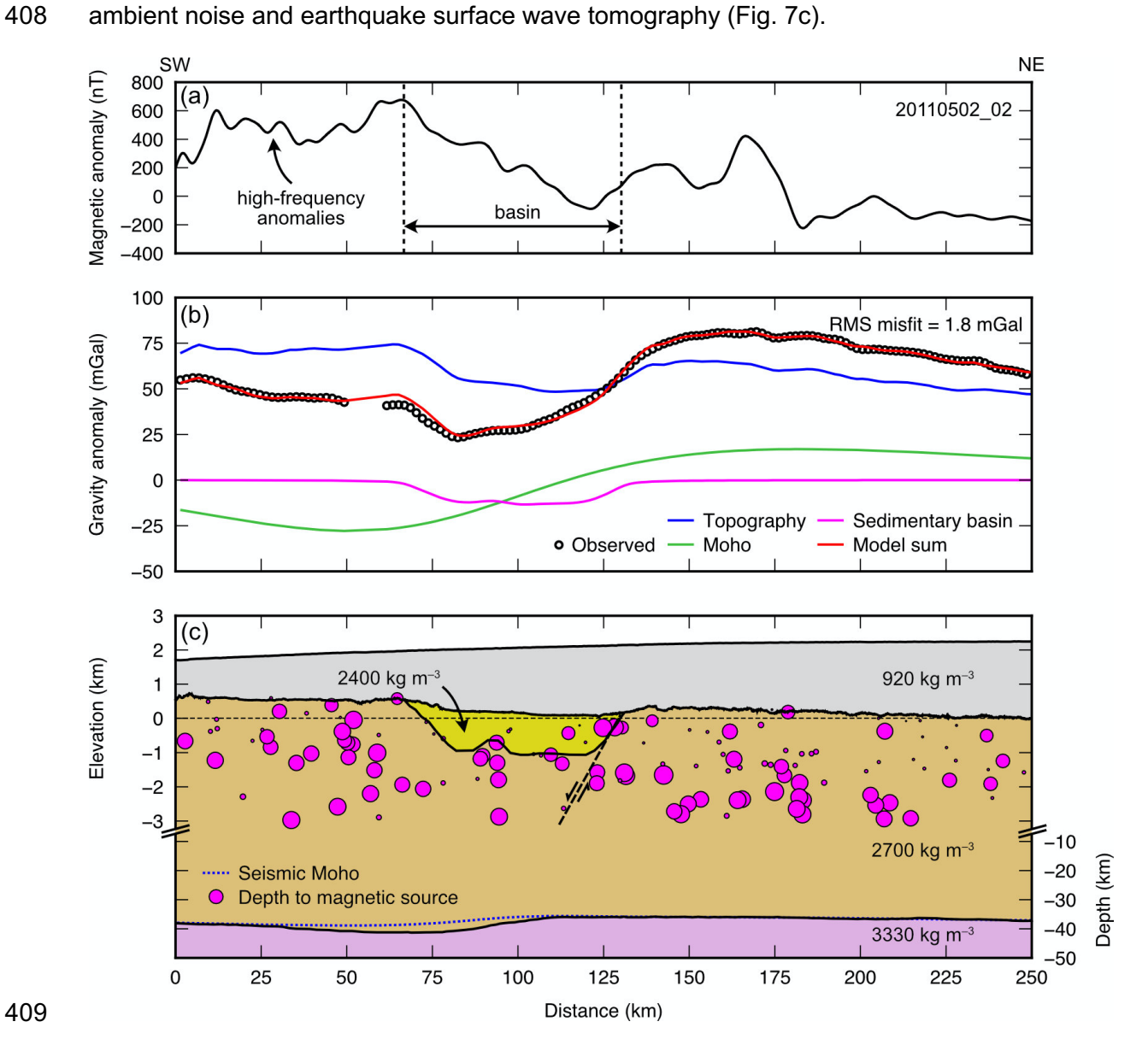


Figure 7. Gravity and magnetic anomalies. (a) Observed magnetic anomaly along OIB flight line 20110502_02 (profile 6 in Fig. 8). Vertical dashed lines mark the boundaries of the sedimentary basin shown in panel c. The magnetic field to the SW of the basin is characterised by a series of high-frequency (~5 km) anomalies. These anomalies are absent over the basin itself. (b) Gravity anomaly modelling. The open circles mark free-air gravity anomaly measurements along the profile (the gap at ~50 km reflects a turn in the flight line, where gravity data are unavailable), and the coloured lines denote the calculated gravity effect associated with the interfaces in our crustal model (panel c). The gravity effect of the topography contains a signal from both the ice surface and bed interfaces. (c) Crustal model associated with the modelled gravity anomaly in panel b. The model comprises the ice sheet, crust, mantle, and a low-density sedimentary basin fill. The black dashed line marks the position of the normal fault as inferred in our flexural modelling (Fig. 6). Magenta circles are estimates of the depth to magnetic source; the radius is scaled to the magnetic susceptibility. The blue dashed line marks the depth of the Moho derived from seismic tomography (Pourpoint et al., 2018).

We then applied the Moho model, which is constrained outside the Camp Century Basin (profile 1 in Fig. 8), to the six gravity models crossing the basin. Moving from NW to SE, we found that a progressively more negative residual gravity anomaly remained over the basin after correcting for the gravity effects of the surface and Moho topography, reaching a maximum residual 'low' of approx. –15 mGal (Fig. 7b, 8a,b). To reconcile this anomaly we forward modelled the geometry of a low-density (2400 kg m⁻³) sedimentary infill within the basin, achieving RMS misfits between the modelled and observed gravity anomaly of <2 mGal (Fig. 7). The maximum modelled thickness of sedimentary material was ~1200 m, with a basin-wide average of ~630 m. We also found that the average thickness of sediment increases from ~80 m (the resolvable limit of the gravity data) at the NW end of the basin to ~910 m in the basin centre (Fig. 8d). The edge of the sedimentary unit coincides with the base of the escarpment at the NE margin of the Camp Century Basin, which is assumed to be the location of the normal fault (Fig. 7). Our gravity models also suggest that the putative impact crater to the NE of the basin also contains a sedimentary infill (~300 m thick), as had been previously hypothesised (Fig. 8d) (MacGregor et al., 2019).

Assuming that the observed gravity anomaly data are accurate to ±1 mGal (Tinto et al., 2019), and the sediment-bedrock density contrast uncertainty is ±100 kg m⁻³, the estimated uncertainty in the modelled sediment thickness ranges from ±80 to ±310 m (Fig. 8d). Although there is significant uncertainty associated with the density contrast between the lower crust and upper mantle, this would largely affect the longer wavelengths (>100 km) of the gravity field, and not the modelled spatial variation in sediment thickness along the basin.

The depth to magnetic source distribution independently derived from Werner deconvolution is broadly consistent with the gravity models, showing a cluster of high-susceptibility sources near the modelled base of the sedimentary basin (Fig. 7c). The magnetic field to the SW of the Camp Century Basin is characterised by a series of high-frequency (~5 km) 100–200 nT anomalies (Fig. 7a), which coincide with a number of shallow

high-susceptibility magnetic sources close to the ice-bed interface (Fig. 7c). These high frequency anomalies and high-susceptibility sources are absent from the basin itself (Fig. 7a), which is consistent with the presence of a non-magnetic sedimentary infill. We note that, given the limits of data resolution and uncertainties in sediment density variation, it is not possible to resolve the finer-scale geometry of the sedimentary basin from airborne gravity data alone.

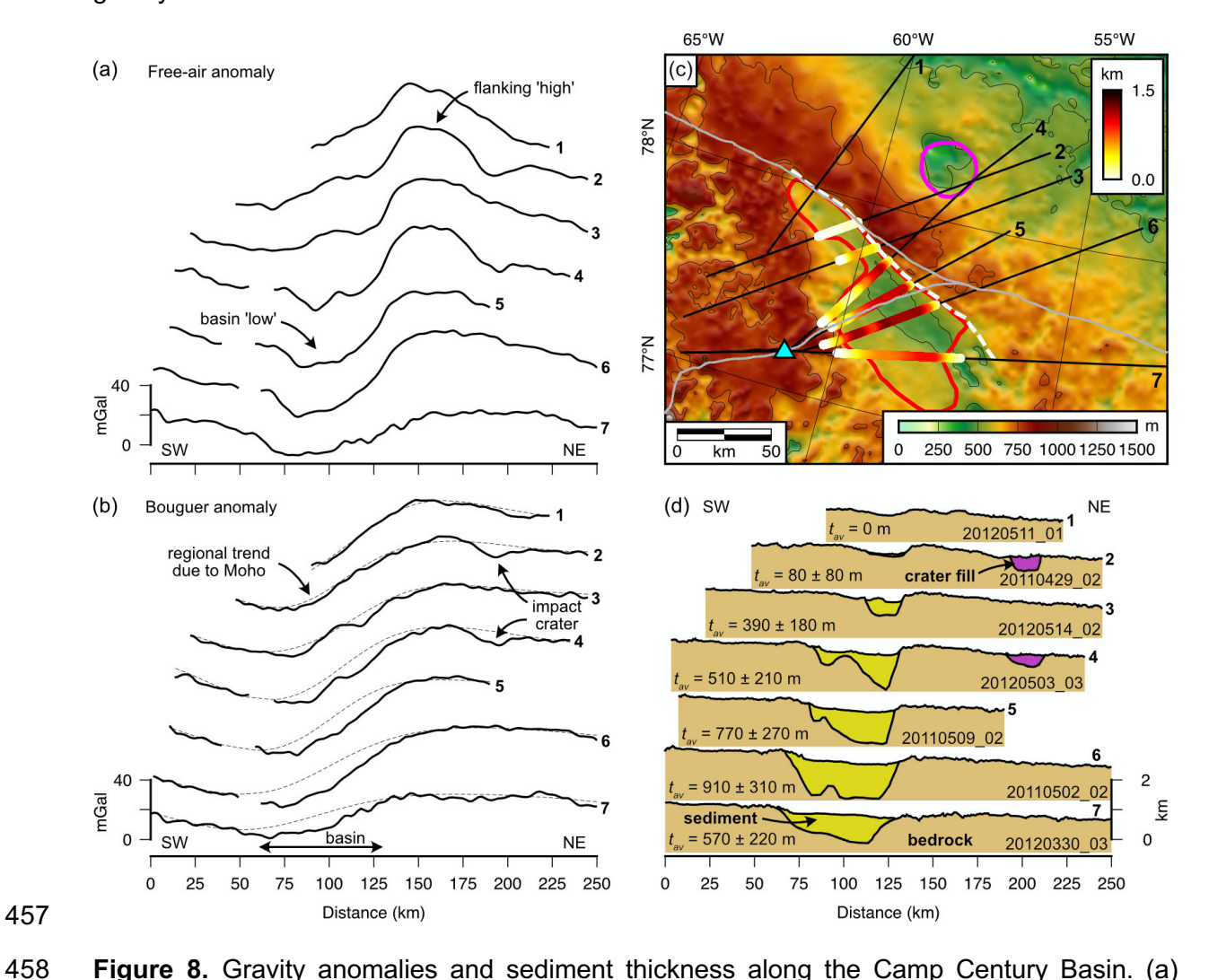


Figure 8. Gravity anomalies and sediment thickness along the Camp Century Basin. (a) Observed free-air anomaly along seven OIB flight lines crossing the Camp Century Basin. The profiles have been aligned relative to the NE margin of the basin. (b) Bouguer anomaly calculated by subtracting the gravity effects of the ice surface and bed topography from the free-air anomaly. The dashed lines mark the regional gravity effect of the modelled deflection of the Moho. Locations where the gravity effect of the Moho exceeds the Bouguer anomaly are indicative of a local mass deficit. (c) Gravity model profiles overlain on the rebounded bed topography. The colour scale shows the modelled sediment thickness along the lines (line 1 is used as a reference line, assumed to contain no sediment). Red outline marks the basin area characterised by low basal and ice surface roughness. White dashed line marks the base of the escarpment. Magenta outline marks the impact crater (MacGregor et al., 2019). Blue triangle marks Camp Century. (d) Modelled sediment thickness along the seven profiles. The average sediment thickness (t_{av}) increases along the basin from ~80 m (the resolvable limit from the gravity anomaly) to ~910 m. Uncertainties placed on the modelled sediment thickness reflect the uncertainty in the observed gravity anomaly and assumed

sediment density. In profiles 2 and 4, a low-density infill has also been modelled within the impact crater (magenta).

5. Discussion

5.1. Landscape development in northwest Greenland

Our geomorphological mapping suggests that a complex network of bedrock channels is preserved in the subglacial landscape of northwest Greenland. The channels exhibit deeply incised V-shaped cross-profiles, high length-to-width ratios, and a complex dendritic branching pattern, all of which are diagnostic characteristics of fluvial valley networks (Grau Galofre and Jellinek, 2017). The pattern of valley incision into the tilted plateau-like surface NE of the Camp Century Basin is typical of fluvial channel incision into a bedrock surface, and likely forms a tributary system to the palaeo-fluvial channels documented upstream of Humboldt Glacier (Livingstone et al., 2017). In addition, several channels can be traced cutting through the escarpment and into the Camp Century Basin. A drainage divide between these two families of channels follows the crest of the flank directly above the basin's NE escarpment (Fig. 3). This indicates that the Camp Century Basin and associated escarpment and tilted flank control the pattern of the preserved palaeo-fluvial drainage network. Assuming that the channel network formed prior to widespread glaciation, this indicates that the basin, escarpment, and tilted flank also pre-date extensive glaciation.

In sufficiently wet climates, lakes commonly develop in topographic depressions formed by fault movement. There are several lines of evidence that lead us to propose that the Camp Century Basin once hosted a surface lake. Our flow routing suggests that the basin is a hydrological sink that would readily accommodate a lake if water were to fall on the landscape (Fig. 4), and the channels that dissect the landscape and can be traced into the Camp Century Basin are evidence of the former existence of running water (Fig. 3). The hydrological lake surface elevation coincides with the terraces and backing cliffs observed along the basin margin (Fig. 4; Supplementary Fig. 3), which closely resemble stepped lacustrine/marine terraces and scarps formed by shoreface erosion (Rovere et al., 2016). The average elevation of these 'palaeo-shoreline' features under ice-free conditions is 653 m above sea level, and the standard deviation of their elevations decreases from 38 to 11 m when the topography is rebounded for ice and lake loading (Fig. 9), implying a common process of formation in the absence of ice.

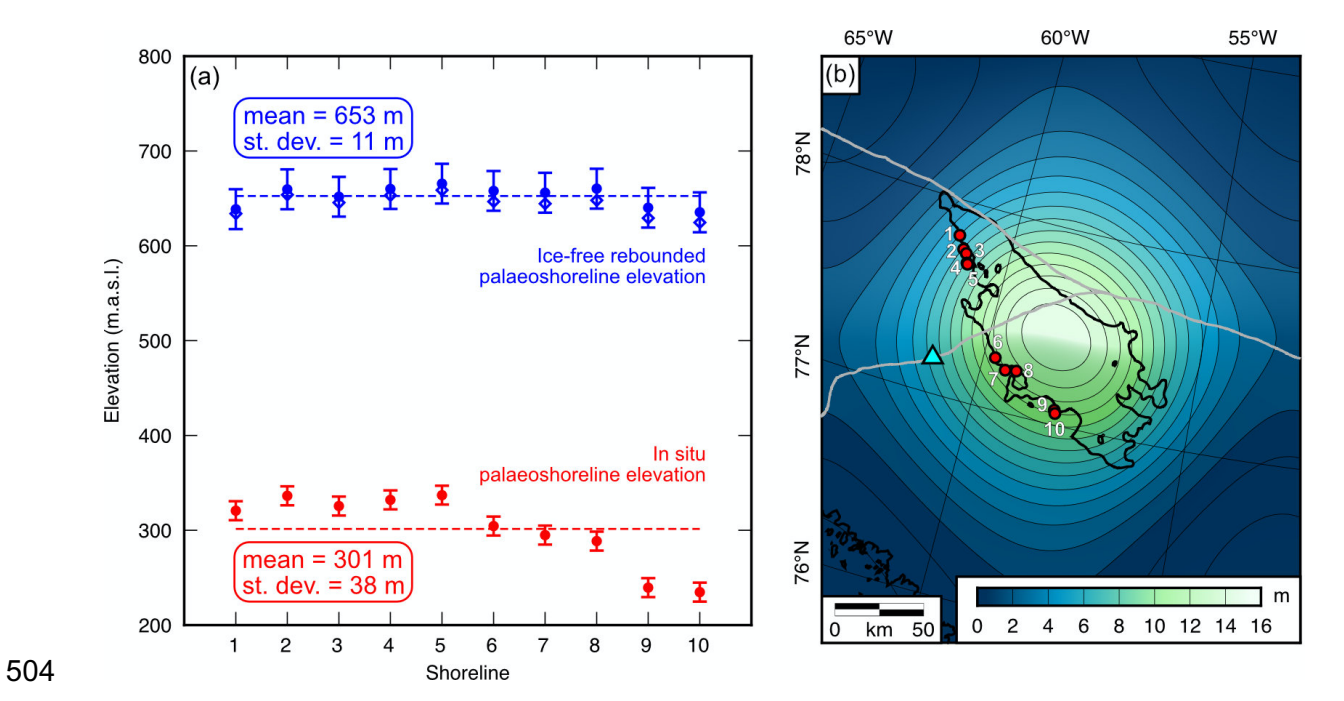


Figure 9. Camp Century Basin palaeoshoreline elevations. (a) Elevations (relative to present-day sea level) of ten palaeoshoreline features observed in OIB RES data (see Fig. 4). Shorelines are numbered moving from NW to SE along the basin. Red = palaeoshoreline elevations observed in situ (beneath the GrIS). Blue = palaeoshoreline elevations when isostatically rebounded for the removal of the modern ice load. Error bars represent the combined uncertainty associated with the radar-derived bed elevation measurements (±10 m) and the isostatic rebound calculation (see Supplementary Fig. 1). Open diamonds show the shoreline elevations corrected for the addition of a lake water load (see panel b). The water loading signal is smaller than the uncertainty associated with the elevation measurements and ice loading signal. Dashed lines mark the mean palaeoshoreline elevation under both scenarios. (b) Deformation associated with water loading in the Camp Century Basin. Contour interval is 1 m. The flexural deformation is computed for the addition of the lake load shown in Fig. 4 assuming a water density of 1000 kg m⁻³ and an effective elastic thickness of 35 km (positive values denote downward displacement due to loading). Black outline marks the modelled lake shoreline. Numbered red circles mark the locations of the palaeoshorelines corresponding with panel a. Blue triangle marks Camp Century; grey lines mark the ice divides.

Additionally, gravity modelling and Werner deconvolution indicate that the basin contains up to ~1.2 km of low-density, non-magnetic sedimentary infill (Fig. 7, 8). The basin is also a contiguous area of smooth bed, with a conspicuous absence of small-scale bed incision compared to the surrounding terrain (Fig. 3). Although smooth subglacial terrain is potentially consistent with either hard bedrock or soft sedimentary material (Cooper et al., 2019; Siegert et al., 2004), the topographic configuration of the basin and the coincidence of smooth topography with the modelled sediment distribution (Fig. 8c) are indicative of a depositional setting, and lend support to the palaeo-lake hypothesis (Fig. 10). In contrast to the smooth terrain across most of the basin, the bed near the hydrological outflow at the southeastern end of the lake is notably rough, resulting in highly variable water depths (Fig. 3a,c, 4a). A potential explanation for this is localised incision of lake-fill sediments and/or

bedrock by outburst flooding from a palaeo- subglacial or glacially dammed lake, as has been suggested as a possible mechanism for landscape modification in Greenland (Keisling et al., 2020) and Antarctica (Jordan et al., 2010).

The average dimensions of the modelled palaeo-lake (Fig. 4a) are approximately 160 km x 45 km, with a surface area of 7,100 km², an average water depth of 82 m, and a volume of ~580 km³. While we hypothesise that the Camp Century Basin hosted water in the past in the form of a subaerial, and/or subglacial, and/or glacially dammed lake, we emphasise that there is a lack of evidence for the existence of a subglacial lake (e.g. bright, flat specular reflectors in RES data) within the basin at the present-day (Bowling et al., 2019). We also note that while gravity data can detect low-density sedimentary material, they cannot distinguish between lithified sedimentary rock, stratified lacustrine sediment, or dilatant subglacial till. Future acquisition of active source seismic data may help to better resolve the nature and thickness of the sediment within the basin (cf. Christianson et al., 2014; Smith et al., 2018).

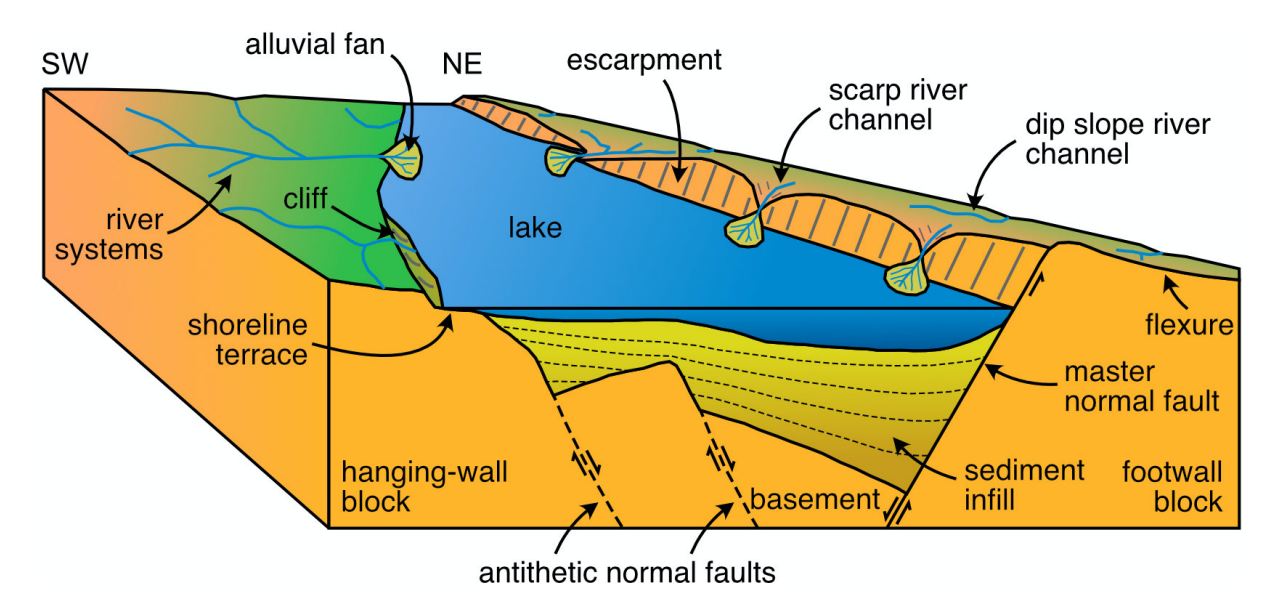


Figure 10. Schematic model of the inferred pre-glacial landscape of our study area in northwest Greenland. Subsidence of the hanging-wall of the normal fault has formed a half-graben-type basin, which accommodates a sedimentary infill and a lake. Subsidence is accommodated by the main normal fault and potentially by a series of antithetic faults in the hanging-wall block. The lake is fed by rivers on the gently sloping hanging-wall side and short, steep rivers that cut through the escarpment on the uplifted footwall side. Flexure of the footwall also allows rivers to drain down the dip-slope away from the Camp Century Basin. Shoreface erosion along the lake has formed a flat terrace backed by a steep cliff.

5.2. Origin of the Camp Century Basin

Our flexural modelling indicates that the asymmetric profile of the Camp Century Basin and the steep escarpment and tilted flank on the NE margin are consistent with a half-graben basin formed by displacement along a normal fault (Fig. 6, 10). Here we consider whether other mechanisms may also be able to account for the observed topography.

One alternative is that the basin was formed by glacial erosion, which can deepen pre-glacial basins/valleys by >1 km (e.g. Petermann Trough; Fig. 1) (Medvedev et al., 2013). However, the maximum amount of erosion within the Camp Century Basin is limited to 300 m (the depth of the basin; Fig. 4), which alone cannot induce sufficient flexural uplift to explain the elevation or tilt of the basin flank (Fig. 6, Supplementary Fig. 4). Formation of the basin by erosion beneath the modern GrIS is also inconsistent with the regional ice sheet dynamics. The Camp Century Basin is situated close to an ice divide, the ice surface velocity over the basin is low (<20 m/yr), and the orientation of the basin is orthogonal to ice flow (Fig. 1). Moreover, this part of ice sheet is 'likely frozen' at the bed (MacGregor et al., 2016). By contrast, major glacial troughs in Antarctica and Greenland are primarily oriented parallel to ice flow (orthogonal to the coast), which facilitates the convergence of warm-based ice flowing from the continental interior to the margin and focussing of enhanced erosion (Kessler et al., 2008). In interior northwest Greenland, we suggest that ice flow is unable to exploit the topography of the Camp Century Basin due to its unfavourable orientation, and that the regional glaciological conditions strongly favour (i) negligible basal erosion rates and (ii) subglacial landscape preservation.

We note however that we cannot fully exclude the possibility of a contribution from erosion beneath early ice sheets with dynamics more conducive to erosion. For example, the presence of sediment at the base of the Camp Century borehole (Christ et al., 2020), situated outside of the main basin depocentre, may be indicative of local erosion and glacial transport of sediment from the palaeo-lake basin or elsewhere. However, it appears improbable that a localised ice mass could accumulate a sufficient ice flux to excavate an interior basin significantly wider than the numerous U-shaped glacial troughs that dissect the coast of northwest Greenland (Fig. 1).

Another possibility is that the high terrain forming an inverted 'V'-shape surrounding the basin (Fig. 3a) resembles the topography typically associated with a plunging bedrock fold structure. However, the regional gravity anomalies do not correlate with a structure of this type, instead showing a linear gravity 'high' trending along the strike of the basin escarpment to the coast (Fig. 7b, Supplementary Fig. 6). This linear gravity 'high' is present in the free-air and Bouguer anomalies, and persists if the gravity anomaly is also corrected for compensation of topography by local crustal thickness variations, indicating that the topography is not primarily supported by Airy isostasy (Supplementary Fig. 6). We suggest that this linear gravity 'high' may mark the continuation of the modelled border fault to the coast, and our gravity modelling indicates that it is consistent with the uplift and compensation of the footwall topography by elastic flexure (Fig. 6c, 7c). Matching the observed flank uplift required a faulted later thickness of ~20 km (Fig. 6), which implies that the modelled fault is a significant crustal scale feature. Although this is difficult to verify

without deep seismic imaging, it is consistent with the length of the escarpment and the wider Airy isostatic gravity anomaly (Supplementary Fig. 6).

Although we have only mapped the location of a single normal fault, the basin configuration may be more complex, potentially involving segmentation of the master fault and/or the presence of subsidiary faults (Fig. 10), as is commonly observed in extensional fault systems. While these smaller-scale details cannot be resolved with the available airborne geophysical data, we suggest that future acquisition of ground-based active source seismic data may allow improved imaging of the geological structure beneath the basin, including a more precise estimate of sediment thickness.

The presence of a normal fault would suggest that northwest Greenland has been subjected to crustal extension in the past. In section 5.1, we inferred that the basin and escarpment were formed prior to widespread glaciation. A lack of contemporary seismic activity (Nettles and Ekström, 2010) also suggests that the fault is not active at the presentday. The Cenozoic regional tectonic history is dominated by the development of a major intercontinental and subsequently oceanic rift system between Greenland and Canada commencing in the Palaeocene-Eocene (Oakey and Chalmers, 2012). Extensional structures in Baffin Bay, including the Melville Bay Graben (Knutz et al., 2015), trend approximately parallel to the Camp Century Basin (Supplementary Fig. 6). This presents the possibility that the Camp Century Basin was formed in association with this episode of extension. Alternatively, northwest Greenland may have been affected by lithospheric heating associated with passage over the Iceland mantle plume. However, a wide range of reconstructed hotspot tracks has been inferred (see e.g. Rogozhina et al., 2016 and references therein), resulting in substantial uncertainty in the hotspot history. Although determining the tectonic history of the Camp Century Basin is beyond the scope of this study. we propose that the basin may provide important constraints for future geophysical modelling studies seeking to understand the tectonic evolution of northwest Greenland.

5.3. Records of past ice sheet extent and palaeoclimate

Glaciation appears not to have significantly modified the pre-glacial geomorphology of the Camp Century Basin and surrounding terrain. The absence of major landscape modification by glacial erosion is potentially significant for preservation of records of past ice sheet extent and palaeoclimate. Although geophysical data alone do not allow us to tightly constrain the age of the landscape, a climate sufficiently warm and wet to support the existence of a palaeo-fluvial network and palaeo-lake in northwest Greenland (Fig. 10) is consistent with evidence for polar forests and high latitude warmth as recent as the Pliocene-early Pleistocene (Funder et al., 2001; Knutz et al., 2015). Assuming typical sedimentation rates of 0.1–1.0 mm/yr, the ~1 km sedimentary succession within the Camp Century Basin would have accumulated over hundred-kyr to Myr timescales. The sedimentary material

preserved within the lake may therefore date from prior to widespread Greenlandic glaciation and/or interglacial periods following ice sheet inception.

Provided with favourable basal conditions (see section 5.2), lake sediments can be preserved beneath ice sheets for millions of years (Briner et al., 2007; Smith et al., 2018). We suggest that the Camp Century Basin may contain a sedimentary record that could (a) indicate whether the region was ice-free or ice covered during past climate intervals, providing valuable constraints on past ice sheet extent (e.g. Briner et al., 2010), and/or (b) provide unique insights into past climate and environmental conditions via analysis of proxies such as micro- and macrofossils, sediment mineralogy and grain size, and isotope concentrations and ratios (e.g. Melles et al., 2012). The Camp Century Basin may therefore be an important site for future sub-ice drilling and the recovery of sediment records that may yield valuable insights into the glacial, climatological, and environmental history of northwest Greenland.

6. Conclusions

In this study, we have examined the Camp Century Basin in northwest Greenland. We have constrained the processes responsible for the development of the subglacial landscape, and their significance for understanding palaeoclimate and ice sheet behaviour. We draw the following conclusions:

- 1. Radio-echo sounding data reveal that the Camp Century Basin is situated beneath ~1.8 km of ice, is approximately 160 km long, 20–60 km wide, and 400 m deep, and is characterised by smooth topography. The basin is asymmetric, with a gently sloping SW margin and a steep linear escarpment along the NE margin. The basin topography controls the organisation of a preserved palaeo-fluvial drainage network, suggesting that the basin pre-dates widespread glaciation in northwest Greenland.
- 2. The morphology of the Camp Century Basin and associated escarpment and uplifted flank are consistent with formation via flexure due to normal faulting. The flank uplift is well explained by a simple elastic plate model with a T_e of ~35 km. Gravity modelling and magnetic depth-to-source analysis also indicate that the basin contains an infill of low-density sedimentary material, with a maximum thickness of ~1.2 km in the basin centre.
- 3. Geomorphological analysis indicates that a palaeo-lake formerly occupied the Camp Century Basin. The palaeo-lake was fed by the palaeo-fluvial drainage network and likely facilitated sediment deposition within the basin. Sedimentary material preserved within the basin may therefore contain valuable records of regional past ice sheet extent and environmental conditions, and may yield important insights into understanding climate and GrIS behaviour during past warm intervals. We therefore propose that the Camp Century Basin may be a promising target for future acquisition

of ground-based active source seismic data and potential recovery of subglacial material by sub-ice drilling.

Acknowledgements

This research was supported by the U.S. National Science Foundation (Navigating the New Arctic; grant number: ICER 19-28146). The Operation IceBridge radar, gravity and magnetic anomaly datasets are archived and freely available at the National Snow and Ice Data Center (NSIDC). Profiles shown in the figures throughout this manuscript are labelled with the Operation IceBridge flight numbers. The gridded BedMachine v.3 bed topography and ice thickness, MEaSUREs ice sheet velocity, and MODIS ice surface imagery data products are also freely available at NSIDC. We would like to extend thanks to Billy D'Andrea, Benjamin Keisling and Joerg Schaefer for valuable discussions during the early drafting of this manuscript, and to the two anonymous reviewers whose constructive comments helped to improve the final manuscript.

Appendix A. Elastic plate flexure calculation

In our flexural models we assumed that the response of the lithosphere to (un)loading of ice/water/rock over geological timescales approximates that of a flexed elastic plate overlying an inviscid substrate (the mantle). We therefore used a flexural isostatic model to determine the vertical displacement of the Earth's surface (w) in response to surface loading (h). Computing the steady-state flexure requires solution of the general 2D flexure equation

$$\nabla^2[D(x,y)\nabla^2w(x,y)] + (\rho_{mantle} - \rho_{infill})gw(x,y) = (\rho_{load} - \rho_{displace})gh(x,y) \tag{A1}$$

692 where

693
$$D(x,y) = \frac{ET_e(x,y)^3}{12(1-v^2)}$$
 (A2)

is the flexural rigidity of the lithosphere as a function of spatial dimensions x and y. Equation A1 shows that loads are supported by a combination of elastic bending forces within the lithosphere and buoyancy forces imparted on the base of the crust by the underlying mantle. E (Young's modulus; 100 GPa) and v (Poisson's ratio; 0.25) are elastic constants, g is the acceleration due to gravity (9.81 m s⁻²), and the density terms (ρ) depend on the particular loading or unloading situation being considered. The densities of the load and the mantle are given by ρ_{load} and ρ_{mantle} respectively. The terms $\rho_{displace}$ and ρ_{infill} describe the densities of the material displaced by the load and the material infilling in the flexure respectively.

For isostatic adjustment over timescales of millions of years, we assume that the isostatic response reaches final elastic steady state, and do not consider transient viscoelastic effects. If the flexural rigidity (i.e. effective elastic thickness) is spatially uniform,

equation A1 can be solved analytically. If the flexural rigidity is spatially variable, the equation is instead solved numerically using a finite difference approach.

We note that our ice unloading calculation (section 3.1) used a spatially variable T_e grid (Steffen et al., 2018) as opposed to the value of 35 km derived from our flexure modelling (section 4.2). However, we compared the modelled flexural uplift due to ice unloading for both scenarios and found that across our study area the difference in uplift between the two scenarios varied by only ~15 m, which is comparable to the error margin in the ice thickness measurements (Supplementary Fig. 1).

In the case of extensional faulting, the hanging-wall block is displaced downwards along the fault plane and unloads the footwall block. This mechanical unloading modifies the regional isostatic balance such that the footwall is uplifted and the system (both blocks) is tilted in an opposing direction to the fault dip (Fig. 6c). Because the lithosphere has a finite rigidity and regional isostatic compensation is achieved through elastic bending forces within the lithosphere and buoyancy forces from the mantle (Equation A1), the region experiences elastic flexure rather than simple block tilting. This results in the characteristic pattern of footwall uplift and hanging-wall subsidence shown in Fig. 6c.

References

707

708

709

710

711

712

713

714

715

716

717

718

719

720

- 722 Bamber, J.L., Siegert, M.J., Griggs, J.A., Marshall, S.J., Spada, G., 2013. Paleofluvial mega-
- canyon beneath the central Greenland ice sheet. Science 341, 997–999.
- 724 doi:10.1126/science.1239794
- 725 Bassett, D., Watts, A.B., 2015. Gravity anomalies, crustal structure, and seismicity at
- subduction zones: 1. Seafloor roughness and subducting relief. Geochemistry,
- 727 Geophys. Geosystems 16, 1508–1540. doi:10.1002/2014GC005684
- 728 Bennike, O., Knudsen, K.L., Abrahamsen, N., Böcher, J., Cremer, H., Wagner, B., 2010.
- Early Pleistocene sediments on Store Koldewey, northeast Greenland. Boreas 39, 603–
- 730 619. doi:10.1111/j.1502-3885.2010.00147.x
- 731 Bierman, P.R., Shakun, J.D., Corbett, L.B., Zimmerman, S.R., Rood, D.H., 2016. A persistent
- and dynamic East Greenland Ice Sheet over the past 7.5 million years. Nature 540,
- 733 256–260. doi:10.1038/nature20147
- Bowling, J.S., Livingstone, S.J., Sole, A.J., Chu, W., 2019. Distribution and dynamics of
- 735 Greenland subglacial lakes. Nat. Commun. 10, 2810. doi:10.1038/s41467-019-10821-w
- 736 Briner, J.P., Axford, Y., Forman, S.L., Miller, G.H., Wolfe, A.P., 2007. Multiple generations of
- interglacial lake sediment preserved beneath the Laurentide Ice Sheet. Geology 35,
- 738 887–890. doi:10.1130/G23812A.1
- 739 Briner, J.P., Stewart, H.A.M., Young, N.E., Philipps, W., Losee, S., 2010. Using proglacial-

- threshold lakes to constrain fluctuations of the Jakobshavn Isbræ ice margin, western
- Greenland, during the Holocene. Quat. Sci. Rev. 29, 3861–3874.
- 742 doi:10.1016/j.quascirev.2010.09.005
- Christ, A., Bierman, P., Dahl-Jensen, D., Steffensen, J., Peteet, D., Thomas, E., Cowling, O.,
- Steig, E., Corbett, L., Schaefer, J., Hidy, A., Caffee, M., Rittenour, T., Tison, J.-L., Blard,
- P.-H., Protin, M., Southon, J., 2020. Camp Century ice core basal sediments record the
- absence of the Greenland Ice Sheet within the last million years. EGU Gen. Assem.
- 747 EGU2020-12. doi:10.5194/egusphere-egu2020-12243
- 748 Christianson, K., Peters, L.E., Alley, R.B., Anandakrishnan, S., Jacobel, R.W., Riverman,
- K.L., Muto, A., Keisling, B.A., 2014. Dilatant till facilitates ice-stream flow in northeast
- 750 Greenland. Earth Planet. Sci. Lett. 401, 57–69. doi:10.1016/j.epsl.2014.05.060
- 751 Cochran, J.R., Burton, B., Frearson, N., Tinto, K., 2012. IceBridge Scintrex CS-3 Cesium
- 752 Magnetometer L1B Geolocated Magnetic Anomalies, Version 1 [WWW Document].
- 753 Boulder, Color. USA. NASA Natl. Snow Ice Data Cent. Distrib. Act. Arch. Cent.
- 754 doi:10.5067/Q1APJXOFVOMB
- Contreras-Reyes, E., Osses, A., 2010. Lithospheric flexure modelling seaward of the Chile
- trench: Implications for oceanic plate weakening in the Trench Outer Rise region.
- 757 Geophys. J. Int. 182, 97–112. doi:10.1111/j.1365-246X.2010.04629.x
- Cooper, M.A., Jordan, T.M., Schroeder, D.M., Siegert, M.J., Williams, C.N., Bamber, J.L.,
- 759 2019. Subglacial roughness of the Greenland Ice Sheet: Relationship with
- contemporary ice velocity and geology. Cryosph. 13, 3093–3115. doi:10.5194/tc-13-
- 761 3093-2019
- Cooper, M.A., Michaelides, K., Siegert, M.J., Bamber, J.L., 2016. Paleofluvial landscape
- inheritance for Jakobshavn Isbræ catchment, Greenland. Geophys. Res. Lett. 43,
- 764 6350–6357. doi:10.1002/2016GL069458
- 765 Dahl-Jensen, T., Larsen, T.B., Woelbern, I., Bach, T., Hanka, W., Kind, R., Gregersen, S.,
- Mosegaard, K., Voss, P., Gudmundsson, O., 2003. Depth to Moho in Greeland:
- Receiver-function analysis suggests two proterozoic blocks in Greenland. Earth Planet.
- 768 Sci. Lett. 205, 379–393. doi:10.1016/S0012-821X(02)01080-4
- Fldrett, J.S., Harding, I.C., Wilson, P.A., Butler, E., Roberts, A.P., 2007. Continental ice in
- 770 Greenland during the Eocene and Oligocene. Nature 446, 176–179.
- 771 doi:10.1038/nature05591
- Funder, S., Bennike, O., Böcher, J., Israelson, C., Petersen, K.S., Símonason, L.A., 2001.
- 1773 Late Pliocene Greenland The Kap København Formation in North Greenland. Bull.
- 774 Geol. Soc. Denmark 48, 117–134.

- Fürst, J.J., Goelzer, H., Huybrechts, P., 2015. Ice-dynamic projections of the Greenland ice
- sheet in response to atmospheric and oceanic warming. Cryosph. 9, 1039–1062.
- 777 doi:10.5194/tc-9-1039-2015
- Grau Galofre, A., Jellinek, A.M., 2017. The geometry and complexity of spatial patterns of
- terrestrial channel networks: Distinctive fingerprints of erosional regimes. J. Geophys.
- 780 Res. Earth Surf. 122, 1037–1059. doi:10.1002/2016JF003825
- Haran, T., Bohlander, J.A., Scambos, T.A., Painter, T., Fahnestock, M.A., 2018. MEaSUREs
- MODIS Mosaic of Greenland (MOG) 2005, 2010, and 2015 Image Maps, Version 2
- 783 [WWW Document]. Boulder, Color. USA. NSIDC Natl. Snow Ice Data Cent.
- 784 doi:10.5067/9ZO79PHOTYE5
- Helland, P.E., Holmes, M.A., 1997. Surface textural analysis of quartz sand grains from ODP
- site 918 off the southeast coast of Greenland suggests glaciation of southern Greenland
- at 11 Ma. Palaeogeogr. Palaeoclimatol. Palaeoecol. 135, 109–121. doi:10.1016/S0031-
- 788 0182(97)00025-4
- Henriksen, N., Higgins, A.K., Kalsbeek, F., Pulvertaft, T.C.R., 2009. Greenland from
- Archaean to Quaternary: Descriptive text to the 1995 Geological map of Greenland,
- 791 1:2500000. 2nd edition. Geol. Surv. Denmark Greenl. Bull. 18, 126.
- Jamieson, S.S.R., Stokes, C.R., Ross, N., Rippin, D.M., Bingham, R.G., Wilson, D.S.,
- Margold, M., Bentley, M.J., 2014. The glacial geomorphology of the Antarctic ice sheet
- 794 bed. Antarct. Sci. 26, 724–741. doi:10.1017/S0954102014000212
- Jordan, T.A., Ferraccioli, F., Corr, H., Graham, A., Armadillo, E., Bozzo, E., 2010. Hypothesis
- for mega-outburst flooding from a palaeo-subglacial lake beneath the East Antarctic Ice
- 797 Sheet. Terra Nov. 22, 283–289. doi:10.1111/j.1365-3121.2010.00944.x
- Joughin, I., Smith, B.E., Howat, I.M., Scambos, T., Moon, T., 2010. Greenland flow variability
- from ice-sheet-wide velocity mapping. J. Glaciol. 56, 415–430.
- 800 doi:10.3189/002214310792447734
- Keisling, B.A., Nielsen, L.T., Hvidberg, C.S., Nuterman, R., DeConto, R.M., 2020. Pliocene-
- Pleistocene megafloods as a mechanism for Greenlandic megacanyon formation.
- 803 Geology 1–5. doi:10.1130/G47253.1
- 804 Kessler, M.A., Anderson, R.S., Briner, J.P., 2008. Fjord insertion into continental margins
- driven by topographic steering of ice. Nat. Geosci. 1, 365–369. doi:10.1038/ngeo201
- Kjær, K.H., Larsen, N.K., Binder, T., Bjørk, A.A., Eisen, O., Fahnestock, M.A., Funder, S.,
- Garde, A.A., Haack, H., Helm, V., Houmark-Nielsen, M., Kjeldsen, K.K., Khan, S.A.,
- 808 Machguth, H., McDonald, I., Morlighem, M., Mouginot, J., Paden, J.D., Waight, T.E.,
- Weikusat, C., Willerslev, E., MacGregor, J.A., 2018. A large impact crater beneath

- Hiawatha Glacier in northwest Greenland. Sci. Adv. 4. doi:10.1126/sciadv.aar8173
- Knutz, P.C., Hopper, J.R., Gregersen, U., Nielsen, T., Japsen, P., 2015. A contourite drift
- 812 system on the Baffin Bay-West Greenland margin linking Pliocene Arctic warming to
- poleward ocean circulation. Geology 43, 907–910. doi:10.1130/G36927.1
- Knutz, P.C., Newton, A.M.W., Hopper, J.R., Huuse, M., Gregersen, U., Sheldon, E.,
- Dybkjær, K., 2019. Eleven phases of Greenland Ice Sheet shelf-edge advance over the
- past 2.7 million years. Nat. Geosci. 12, 361–368. doi:10.1038/s41561-019-0340-8
- Koenig, S.J., Dolan, A.M., De Boer, B., Stone, E.J., Hill, D.J., Deconto, R.M., Abe-Ouchi, A.,
- Lunt, D.J., Pollard, D., Quiquet, A., Saito, F., Savage, J., Van De Wal, R., 2015. Ice
- sheet model dependency of the simulated Greenland Ice Sheet in the mid-Pliocene.
- 820 Clim. Past 11, 369–381. doi:10.5194/cp-11-369-2015
- Livingstone, S.J., Chu, W., Ely, J.C., Kingslake, J., 2017. Paleofluvial and subglacial channel
- networks beneath Humboldt Glacier, Greenland. Geology 45, 551–554.
- 823 doi:10.1130/G38860.1
- MacGregor, J.A., Bottke, W.F., Fahnestock, M.A., Harbeck, J.P., Kjær, K.H., Paden, J.D.,
- Stillman, D.E., Studinger, M., 2019. A Possible Second Large Subglacial Impact Crater
- in Northwest Greenland. Geophys. Res. Lett. 46, 1496–1504.
- 827 doi:10.1029/2018GL078126
- MacGregor, J.A., Fahnestock, M.A., Catania, G.A., Aschwanden, A., Clow, G.D., Colgan,
- 829 W.T., Gogineni, S.P., Morlighem, M., Nowicki, S.M.J., Paden, J.D., Price, S.F.,
- Seroussi, H., 2016. A synthesis of the basal thermal state of the Greenland Ice Sheet. J.
- 831 Geophys. Res. Earth Surf. 121, 1328–1350. doi:10.1002/2015JF003803
- 832 Medvedev, S., Souche, A., Hartz, E.H., 2013. Influence of ice sheet and glacial erosion on
- passive margins of Greenland. Geomorphology 193, 36–46.
- 834 doi:10.1016/j.geomorph.2013.03.029
- 835 Melles, M., Brigham-Grette, J., Minyuk, P.S., Nowaczyk, N.R., Wennrich, V., DeConto, R.M.,
- Anderson, P.M., Andreev, A.A., Coletti, A., Cook, T.L., Haltia-Hovi, E., Kukkonen, M.,
- Lozhkin, A. V., Rosen, P., Tarasov, P., Vogel, H., Wagner, B., 2012. 2.8 Million Years of
- Arctic Climate Change from Lake El'gygytgyn, NE Russia. Science 337, 315–320.
- 839 doi:10.1126/science.1222135
- Miller, K.G., Browning, J. V, Schmelz, W.J., Kopp, R.E., Mountain, G.S., Wright, J.D., 2020.
- 841 Cenozoic sea-level and cryospheric evolution from deep-sea geochemical and
- continental margin records. Sci. Adv. 6.
- Morlighem, M., Williams, C.N., Rignot, E., An, L., Arndt, J.E., Bamber, J.L., Catania, G.,
- Chauché, N., Dowdeswell, J.A., Dorschel, B., Fenty, I., Hogan, K., Howat, I., Hubbard,

- A., Jakobsson, M., Jordan, T.M., Kjeldsen, K.K., Millan, R., Mayer, L., Mouginot, J.,
- Noël, B.P.Y., O'Cofaigh, C., Palmer, S., Rysgaard, S., Seroussi, H., Siegert, M.J.,
- Slabon, P., Straneo, F., van den Broeke, M.R., Weinrebe, W., Wood, M., Zinglersen,
- K.B., 2017. BedMachine v3: Complete Bed Topography and Ocean Bathymetry
- Mapping of Greenland From Multibeam Echo Sounding Combined With Mass
- 850 Conservation. Geophys. Res. Lett. 44, 11,051-11,061. doi:10.1002/2017GL074954
- Nettles, M., Ekström, G., 2010. Glacial Earthquakes in Greenland and Antarctica. Annu. Rev.
- 852 Earth Planet. Sci. 38, 467–491. doi:10.1146/annurev-earth-040809-152414
- Oakey, G.N., Chalmers, J.A., 2012. A new model for the Paleogene motion of Greenland
- 854 relative to North America: Plate reconstructions of the Davis Strait and Nares Strait
- regions between Canada and Greenland. J. Geophys. Res. Solid Earth 117, 1–28.
- 856 doi:10.1029/2011JB008942
- Olive, J.A., Behn, M.D., Malatesta, L.C., 2014. Modes of extensional faulting controlled by
- 858 surface processes. Geophys. Res. Lett. 41, 6725–6733. doi:10.1002/2014GL061507
- Paden, J., Li, J., Leuschen, C., Rodriguez-Morales, F., Hale, R., 2019. IceBridge MCoRDS
- L2 Ice Thickness, Version 1 [WWW Document]. Boulder, Color. USA. NASA Natl. Snow
- lce Data Cent. Distrib. Act. Arch. Cent. doi:10.5067/GDQ0CUCVTE2Q
- Pattyn, F., Ritz, C., Hanna, E., Asay-Davis, X., DeConto, R., Durand, G., Favier, L., Fettweis,
- X., Goelzer, H., Golledge, N.R., Kuipers Munneke, P., Lenaerts, J.T.M., Nowicki, S.,
- Payne, A.J., Robinson, A., Seroussi, H., Trusel, L.D., van den Broeke, M., 2018. The
- 865 Greenland and Antarctic ice sheets under 1.5 °C global warming. Nat. Clim. Chang. 8,
- 866 1053–1061. doi:10.1038/s41558-018-0305-8
- Pourpoint, M., Anandakrishnan, S., Ammon, C.J., Alley, R.B., 2018. Lithospheric Structure of
- 868 Greenland From Ambient Noise and Earthquake Surface Wave Tomography. J.
- 869 Geophys. Res. Solid Earth 123, 7850–7876. doi:10.1029/2018JB015490
- 870 Rogozhina, I., Petrunin, A.G., Vaughan, A.P.M., Steinberger, B., Johnson, J. V., Kaban,
- M.K., Calov, R., Rickers, F., Thomas, M., Koulakov, I., 2016. Melting at the base of the
- Greenland ice sheet explained by Iceland hotspot history. Nat. Geosci. 9, 366–369.
- 873 doi:10.1038/ngeo2689
- 874 Ross, N., Jordan, T.A., Bingham, R.G., Corr, H.F.J., Ferraccioli, F., Le Brocq, A.M., Rippin,
- 875 D.M., Wright, A.P., Siegert, M.J., 2014. The Ellsworth Subglacial Highlands: Inception
- and retreat of the West Antarctic Ice Sheet. Geol. Soc. Am. Bull. 126, 3–15.
- 877 doi:10.1130/B30794.1
- 878 Rovere, A., Raymo, M.E., Vacchi, M., Lorscheid, T., Stocchi, P., Gómez-Pujol, L., Harris,
- D.L., Casella, E., O'Leary, M.J., Hearty, P.J., 2016. The analysis of Last Interglacial

- 880 (MIS 5e) relative sea-level indicators: Reconstructing sea-level in a warmer world. 881 Earth-Science Rev. 159, 404–427. doi:10.1016/j.earscirev.2016.06.006 882 Schaefer, J.M., Finkel, R.C., Balco, G., Alley, R.B., Caffee, M.W., Briner, J.P., Young, N.E., 883 Gow, A.J., Schwartz, R., 2016. Greenland was nearly ice-free for extended periods 884 during the Pleistocene. Nature 540, 252-255. doi:10.1038/nature20146 885 Shepard, M.K., Campbell, B.A., Bulmer, M.H., Farr, T.G., Gaddis, L.R., Plaut, J.J., 2001. The 886 roughness of natural terrain: A planetary and remote sensing perspective. J. Geophys. 887 Res. Planets 106, 32777-32795. doi:10.1029/2000JE001429 888 Siegert, M.J., Taylor, J., Payne, A.J., Hubbard, B., 2004. Macro-scale bed roughness of the 889 Siple Coast ice streams in West Antarctica. Earth Surf. Process. Landforms 29, 1591-890 1596. doi:10.1002/esp.1100 891 Smith, A.M., Woodward, J., Ross, N., Bentley, M.J., Hodgson, D.A., Siegert, M.J., King, E.C., 892 2018. Evidence for the long-term sedimentary environment in an Antarctic subglacial 893 lake. Earth Planet. Sci. Lett. 504, 139-151. doi:10.1016/j.epsl.2018.10.011 894 Steffen, R., Audet, P., Lund, B., 2018. Weakened Lithosphere Beneath Greenland Inferred 895 From Effective Elastic Thickness: A Hot Spot Effect? Geophys. Res. Lett. 45, 4733-896 4742. doi:10.1029/2017GL076885 897 The Imbie Team, 2020. Mass balance of the Greenland Ice Sheet from 1992 to 2018. Nature 898 579, 233–239. doi:10.1038/s41586-019-1855-2 899 Tinto, K., Bell, R.E., Cochran, J.R., 2019. IceBridge Sander AIRGrav L1B Geolocated Free 900 Air Gravity Anomalies, Version 1 [WWW Document]. Boulder, Color. USA. NASA Natl. 901 Snow Ice Data Cent. Distrib. Act. Arch. Cent. doi:10.5067/R1RQ6NRIJV89 902 Tripati, A., Darby, D., 2018. Evidence for ephemeral middle Eocene to early Oligocene 903 Greenland glacial ice and pan-Arctic sea ice. Nat. Commun. 9, 1–11. 904 doi:10.1038/s41467-018-03180-5 905 van der Veen, C.J., Leftwich, T., von Frese, R., Csatho, B.M., Li, J., 2007. Subglacial 906 topography and geothermal heat flux: Potential interactions with drainage of the 907 Greenland ice sheet. Geophys. Res. Lett. 34, 1-5. doi:10.1029/2007GL030046 908 Watts, A.B., 2001. Isostasy and Flexure of the Lithosphere. Cambridge University Press, 909 Cambridge. 910 Weertman, J., 1968. Comparison between measured and theoretical temperature profiles of 911 the Camp Century, Greenland, Borehole. J. Geophys. Res. 73, 2691–2700. 912 doi:10.1029/JB073i008p02691
 - Weissel, J.K., Karner, G.D., 1989. Flexural uplift of rift flanks due to mechanical unloading of

914	the lithosphere during extension. J. Geophys. Res. Solid Earth 94, 13919–13950.
915	doi:10.1029/JB094iB10p13919
916	Zwally, H.J., Giovinetto, M.B., Beckley, M.A., Saba, J.L., 2012. Antarctic and Greenland
917	Drainage Systems [WWW Document]. GSFC Cryospheric Sci. Lab. URL
918	http://icesat4.gsfc.nasa.gov/cryo_data/ant_grn_drainage_systems.php (accessed
919	2.1.20).
920	